Pergamon

Int. J. Heat Mass Transfer. Vol. 39, No. 18, pp. 3959–3975, 1996
Copyright © 1996 Elsevier Science Ltd
Printed in Great Britain. All rights reserved
0017–9310/96 $15.00+0.00

PII: S0017–9310(96)00053–1

Analysis of heat transfer with liquid–vapor phase change in a forced-flow fluid moving through porous media

O. RAHLI, F. TOPIN, L. TADRIST and J. PANTALONI

Institut Universitaire des Systèmes Thermiques Industriels (I.U.S.T.I.), Laboratoire des Systèmes
Energétiques et Transferts Thermiques: UMR CNRS 139, Université de Provence, Centre de
St Jerome, Case 162, Av. Escadrille Normandie Niemen, 13397 Marseille Cedex 20, France

(*Received* 16 *June* 1995 *and in final form* 25 *November* 1995)

Abstract—This study focuses on the experimental analysis of transient-regime heat transfer with liquid–vapor phase change in a fluid as it flows through a porous media composed of small bronze spheres. Three distinct zones can be observed: liquid, two-phase and superheated vapor. The boundaries between these zones are determined using temperature and pressure fields. An N-shaped profile is observed for the temperature values along the main flow axis. The first local maximum value on the temperature curve corresponds to the boundary between the liquid zone and the two-phase zone. When a local minimum temperature exists, it corresponds to the boundary between the two-phase and the vapor zones. A finite-element numerical simulation is used to predict the saturation field, which is numerically determined from the boundaries of the two-phase zone and of the experimental temperature field. The liquid and vapor pressure fields are then deduced for all three phase zones of the porous medium. Copyright © 1996 Elsevier Science Ltd.

1. INTRODUCTION

During the last two decades, a great deal of research has been carried out on porous media. This field has gone through a rapid acceleration owing to widespread concern about issues such as energy conservation and environmental pollution. The areas of application include insulation for buildings and equipment, energy storage and recovery, geothermal storage, nuclear waste disposal, chemical reactor design and the storage of heat-generating substances.

Boiling in porous media differs from that observed in open containers, yet few experimental studies have been carried out on this field despite their practical and theoretical interest. Most previous studies have focused primarily on the boiling of a stagnant liquid. It was not until the 1980s that serious efforts were made to develop numerical models for these media, due to considerable progress in computing techniques. Most previous studies have been one-dimensional, dealing mainly with problems of thermal migration or phase change without forced flow [1].

The experiments in refs. [2, 3] have shown that the liquid regime temperature profile can be either conductive or convective. Liquid and vapor counter percolation carries heat across the two-phase zone (the liquid evaporates at the heating surface and the vapor condenses at the boundary between the liquid zone and two-phase zone). Experimental studies suggest that the thermal convection in the liquid region can occur either before or after the onset of boiling. Experiments on visualization [4] reveal that the streamlines of the liquid region penetrate the two-phase zone after the onset of convection.

Schubert and Strauss [5] noted that convection can also be caused by an unstable phase-change mechanism. If steam and liquid water are in thermal equilibrium, thermal disturbances will cause pressure variations which, in turn, will tend to move the fluid against the frictional resistance of the medium. In accordance with the law of mass conservation, horizontal expansion must be accompanied by vertical contraction, implying that the phase change will occur so that vertical forces remain balanced.

In ref. [6], they also studied the stability of vapor-dominant systems with a liquid region overlying a dry vapor region. Their analysis suggests that such systems will remain stable, provided that the permeability is sufficiently slight.

O'Sullivan [7, 8] described certain numerical experiments, after developing a model geothermal reservoir with a variable heat input at the base of a selected layer. As the heat input is increased, the flow type changes a number of times (simple conduction, single-phase convection, convection with an increasingly large boiling zone, and finally irregular oscillatory convection).

The onset of two-dimensional roll convection was studied by Ramesh and Torrance [9] using linear stability analysis. They assumed that the relative permeabilities of liquid and vapor were linear functions of the liquid saturation S. Their analysis reveals that the most important parameters are the dimensionless heat flux at the lower boundary and the Rayleigh numbers for the liquid and two-phase zones.

NOMENCLATURE

d_h	$d_h = \frac{2}{3}\frac{\varepsilon}{1-\varepsilon}d_p$ [m]
d_p	diameter of the spheres [m]
g	acceleration of gravity [m s^{-2}]
K	permeability [m^2]
$\dot{m}$	phase change rate [kg m^{-3} s^{-1}]
P	pressure [Pa]
Pc	capillary pressure [Pa]
Re	Reynolds number for porous medium: $Re = \frac{Ud_m}{\nu}$
S	saturation
S_{irr}	irreducible saturation
T	temperature [°C]
t	time [s]
U	average velocity of the fluid in the porous medium [m s^{-1}]
x, y, z	Cartesian coordinates.

Greek letters

ε	porosity
ϕ	diameter [m]
λ	thermal conductivity [W m^{-1} K^{-1}]
ν	cinematic viscosity [m^2 s^{-1}]
η	mass flow rate [kg m^{-2} s^{-1}]
ρ	density [kg m^{-3}]
σ	surface tension [N m^{-1}].

Subscripts

c	capillary
d	diphasic
eff	effective
irr	irreducible
l	liquid
s	solid
sat	saturation
v	vapor.

Naik and Dhir [10] started looking into the temperature and pressure evolutions of a coolant that evaporates as it flows through a bed of steel spheres (∅ 590–4763 μm) volumically heated by induction. A theoretical model was then developed for the temperature profile in the two-phase liquid zone. Vapor channels were observed in the porous layers of the bed (∅ < 1600 μm) and semi-empirical models were suggested as models of the pressure drop in the two-phase zone.

Tung and Dhir [11] developed a resolution based on two-dimensional finite-element equations (mass and movement equations) for two-phase flow through a heated porous medium. Solutions were also proposed for the cases in which the channels were heated or partially obstructed. The drying fluxes for the one-dimensional case were compared to the values found in previous studies. In the case of a partially-heated axis-symmetrical channel, these authors showed that the behavior is very nearly one-dimensional for the vapor zone and that the liquid tends to move towards the two-phase zone.

The purpose of the present study is to gain a better understanding of boiling mechanisms in porous media with forced flow. The heat transfer and boiling of a liquid in a porous medium were studied using a vertical parellelepiped box filled with stacked spheres and heated on both sides, with a fluid flowing from bottom to top within which temperature, pressure and saturation parameters were analyzed.

2. MATERIALS AND METHODS

The porous medium used was composed of small bronze spheres (∅ = 140–160 μm) held inside a parallelepiped fluoride plastic (PVDF) enclosure with a low thickness-to-width ratio [Fig. 1(a)]. The stacked spheres were held inside the enclosure by sintered consolidations formed of identical spheres and fitted on both ends of the column. The large heating surfaces were formed of bronze plates screwed into the PVDF box and an O-joint to seal the box.

The bronze plates were heated by electrical resistances embedded in a ceramic block. Copper plates were inserted between the heaters and the bronze plates to ensure an even temperature distribution across the large surfaces. The entire enclosure is insulated with compressed asbestos. The energy balance is checked for each experiment. The overall losses were found to be negligible (<3%) and the heat flux is indeed transferred to the fluid [12].

The liquid (i.e. n-pentane) flows through the sintered porous media and then vertically from bottom to top. Average velocity of the liquid, effective heat flux and temperature at the inlet were all monitored and held constant during the experiments.

The average liquid velocity in this study does not exceed 2×10^{-3} m s^{-1}. The Reynolds numbers in the porous medium are less than 1 for the liquid flow, and less than 5 for the vapor flow. In such conditions, the flow is laminar and Darcy's law can be applied [13].

Inlet and outlet pressure values were recorded using two pressure sensors. The temperature values within the porous medium were measured using 130 thermoelectrical sensors (chromel–alumel: ∅ = 0.8 mm) arranged for an optimal coverage of the enclosed volume and connected to a data-acquisition system. Local temperature measurements and polynomial interpolation functions along the vertical and horizontal axes were then used to represent the isotherms and/or the temperature field throughout the entire volume [12, 14].

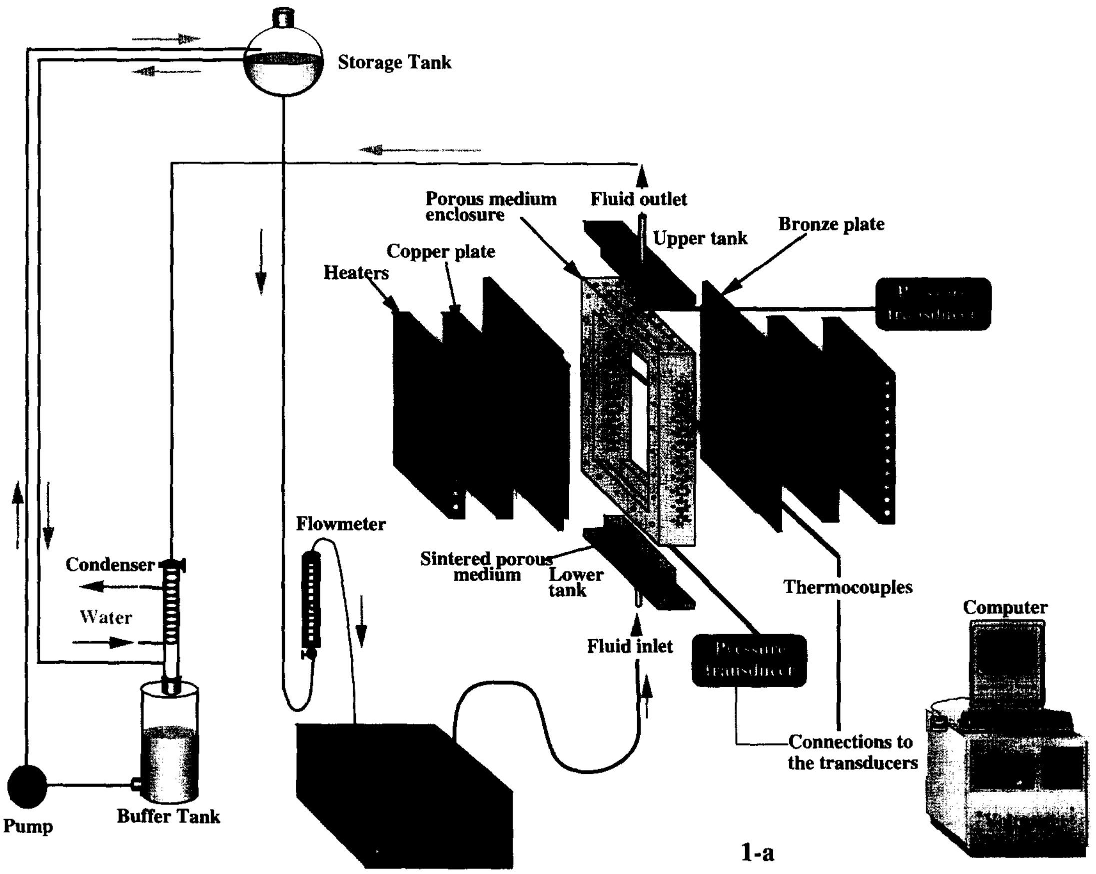

Porous medium dimension	
Height (ZZ) :	0.2 m
Breadth (YY) :	0.1 m
Thickness (XX) :	0.02 m

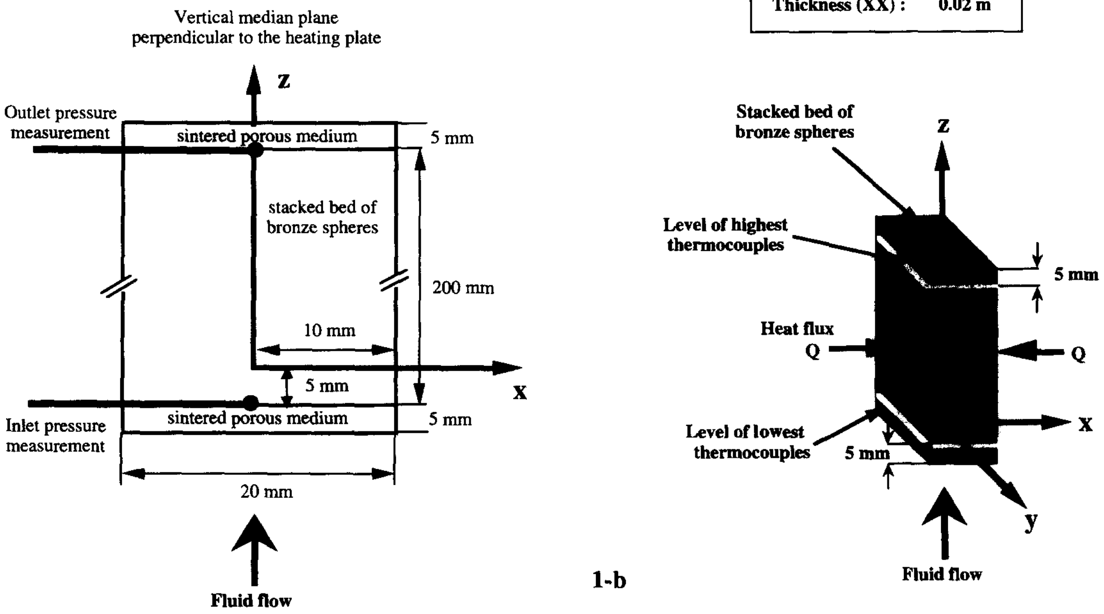

Fig. 1. Schematic diagram of the experimental apparatus to measure the temperature field and pressure drop in a porous medium. (a) Global view of the apparatus. The enclosure containing the porous medium is insulated on all sides by compressed asbestos. (b) Position of the axis, dimensions of the porous medium and of the two-phase zone.

The origin of the coordinate axes is placed at the center of the median plane perpendicular to the heating plates located 5 mm above the inlet sintered consolidation [i.e. at the same height as the lowest thermocouples Fig. 1(b)].

Once all noncondensable substances have been eliminated from the porous medium, the liquid flow is maintained at constant temperature and velocity for approximately 2 h. When the desired temperature has been reached throughout the column, the lateral plates are heated using electrical resistances of which heat flux is maintained constant. Temperature, pressure and flow values are recorded during the whole experiment (i.e. 5 h).

3. EXPERIMENTAL RESULTS

A series of experiments were carried out using an effective heat flux ranging from 2000 to 10 000 W m^{-2} and liquid flow rates ranging from 0.55 to 3.33 cm^3 s^{-1}. The temperature field for the porous medium can be determined at any moment for a given heat flux and flow conditions. In all situations, a stationary regime was obtained after a delay ranging from 1 to 3 h (this span of time is proportionally shorter when the power-to-flow ratio is weak).

Previous studies have confirmed the two-dimensional nature of such phenomena [15], thus only those results for the median plane perpendicular to the heating plates are presented in this paper.

3.1. *Description of the temperature field*

Figure 2 shows the temperature variations $T(x, z)$ at the beginning of the experiment (stationary state with a heat flux of 5000 W m^{-2} and a fluid flow of 2 l/h). At $t = 30$ min, the temperature field reveals a liquid phase flow; and $t = 211$ min (stationary regime) liquid, two-phase and vapor zones are observed. The temperature gradients of each zone are represented using different-colored isothermal ranges and the temperature profiles along XX and ZZ axes using the 'wire frame' grid representation. A stationary regime is obtained after approximately 3 h, thereafter the temperature fields remain the same. The inlet temperature and pressure values are $T = 10$°C and $P = 1.025$ bar. At the outlet, the following values were measured: $T = 37.5$°C and $P = 0.98$ bar.

When there is no phase change, the temperature increases rapidly in the inlet zone and then more slowly toward the outlet of the column. When phase change does occur, the behavior remains roughly unchanged in the inlet zone. It is followed by a zone with decreasing temperatures and then by another zone in which the temperature increases once again, if the heat flux is high enough.

Figure 3 shows the temperature profiles along the XX-axis for stationary conditions at different heights (Z). The profiles show a more or less pronounced 'U' shape, depending on the state of the fluid in the column. These profiles reveal different types of behavior: single-phase liquid and vapor zones having high-amplitude profiles, and the two-phase zone a relatively flat profile. At the inlet, the temperature profile is flat. In the liquid zone, the temperature increases considerably along the XX-axis between the central axis and the wall ($[T_w - T_c] \approx 20$°C, $z = 1$ cm); the difference in temperature values between the wall and the central axis decreases considerably as a function of the distance Z. In the two-phase zone, a nearly flat profile is observed ($[T_w - T_c] \approx 2$°C, $6 \leqslant Z \leqslant 11$ cm). The profile starts to drop again in the single-phase zone as it approaches the outlet ($T_w - T_c) \approx 10$°C.

When no boiling occurs, the velocity and pressure profiles are obtained directly for the entire porous medium applying Darcy's law to inlet and outlet pressure readings. When a phase change does occur, determining the pressure and velocity fields requires the identification of zone boundaries and of their spatial and temporal evolution. Two different approaches were developed to identify these boundaries: one was based on the use of the experimental temperature field and the other relied on pressure and thermodynamic data.

3.2. *Identification of zone boundaries using the temperature fields*

The longitudinal temperature profiles for the different abscissa ($X = -1, -0.8, -0.6, -0.4, -0.2, 0, 0.2, 0.4, 0.6, 0.8, 1$ cm relative to the median axis) are given in Fig. 4 at a stationary regime. The temperature profiles are nearly symmetrical in relation to the median plane (parallel to the heating plates [$X = 0$]). For this reason the profiles are represented in pairs.

The profiles for the different abscissa present roughly the same shape; three distinct zones defined by the distance Z are clearly visible:

(1) A section with increasing values. This is the liquid zone Z_l, in which the temperature increases continuously from the inlet and shows an asymptotic tendency.

(2) A section with decreasing values, corresponding to the two-phase zone Z_d. The beginning of the zone corresponds to the maximum profile at the liquid front and the end to a sharp change in slope, the local minimum temperature at the vapor front.

(3) A third section with increasing values once again. This is the single-phase vapor zone Z_v. This zone is not always present, depending on the experimental conditions (Fig. 5).

The two-phase zone Z_d increases in size as one moves towards the central axis of the column. This can be attributed to the decrease in heat flux moving away from the heating plates. The flux at the walls is used up for the phase change and is then transported along the Z-axis. As a result, the flux decreases from the walls towards the central axis. So does the temperature. It decreases more and more sharply in the

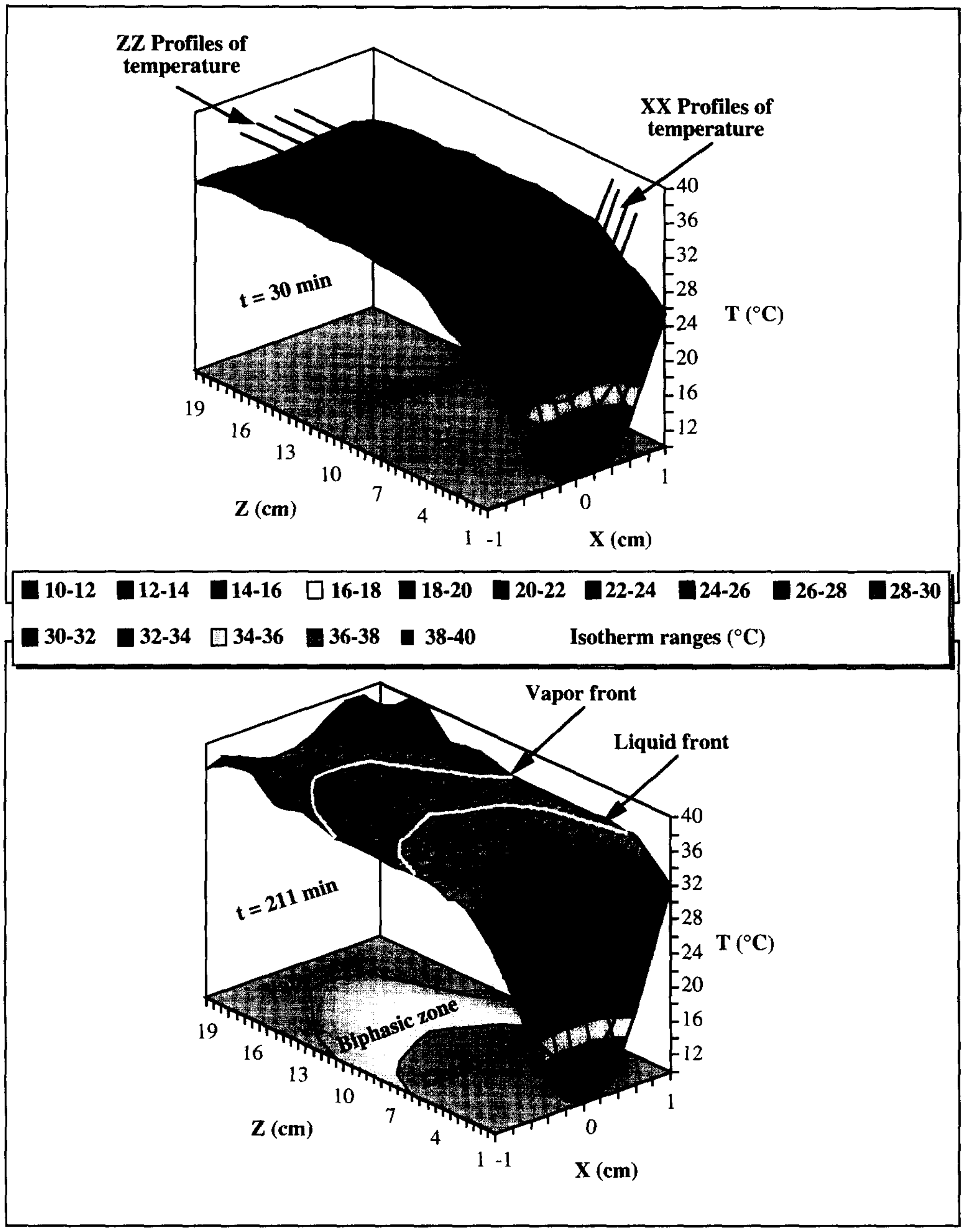

Fig. 2. Temperature field in the median plane perpendicular to the heating plates. Single-phase (transient regime) and two-phase flow (stationary regime). Liquid: n-pentane ($U = 0.69\ 10^{-3}$ m s^{-1}). Heat flux applied to the plates = 5000 W m^{-2}.

two-phase zone, most probably as a result of flow effects.

Figure 5 shows the evolution over time of the temperature profiles along the central axis ($X = 0$) for several experimental flow rate and heat flux conditions. Depending on the flow rate and the heat flux, a stationary regime was obtained with or without phase change and with or without superheating. The different zones tended to keep a similar behavior when experimental conditions were changed.

The detailed representation shows a decreasing temperature profile in the two-phase zone at different moments. This behavior is roughly the same, regardless of the presence or absence of a vapor zone. The two-phase zone decreases in length and temperature until a stationary regime is reached. Along the central axis, the temperature decrease between the liquid front and the vapor front is found to vary under different experimental conditions, and the length of the two-phase zone is proportional to the flow rate.

The heat flux entering the two-phase zone is used up for the phase change. Flow effects cause a pressure drop which in turn induces a temperature decrease, allowing the fluid to remain saturated (P_{sat}, T_{sat}). This

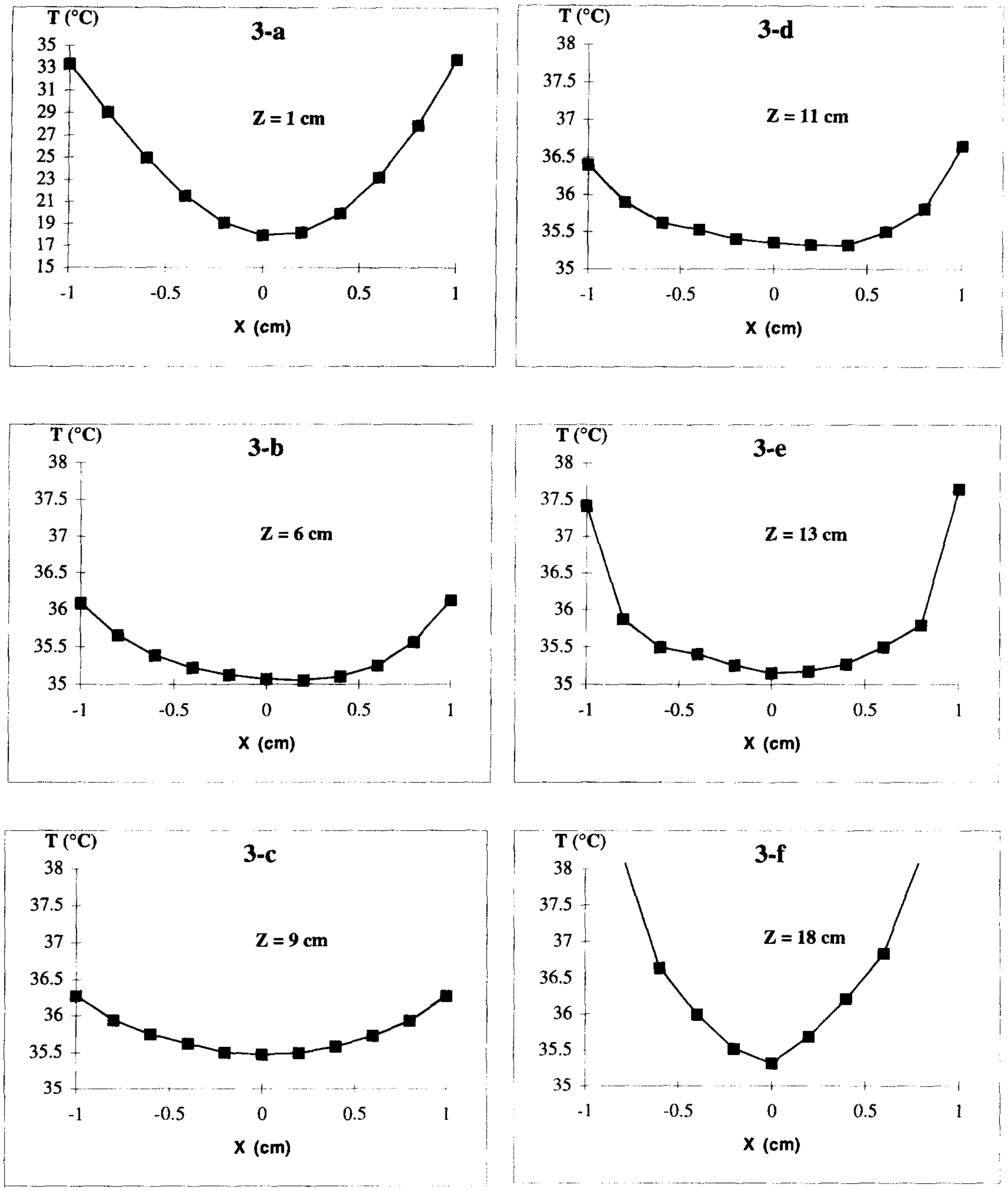

Fig. 3. Temperatures profiles along the horizontal axis in the median plane perpendicular to the heating plates for several values of z at stationary regime. Liquid: n-pentane ($U = 0.69\ 10^{-3}$ m s^{-1}). Heat flux applied to the plates: 5000 W m^{-2}.

phenomenon causes saturation variations which lead to an increased pressure drop, which lasts until a single-phase vapor zone is reached. The pressure gradient increases continuously in the two-phase zone (from the value for the single-phase liquid zone to that of the single-phase vapor zone). This corroborates the behavior shown in Fig. 6, in which the pressure of the liquid and vapor phase are plotted for the entire porous medium. Agreement is found both for intersection points and for slope at these points.

Three distinct zones are observed in stationary state: a liquid zone, a two-phase zone and a vapor zone. Each of these zones can be characterized by a different type of behavior (in terms of both temperature and pressure). The shape of the profiles is largely affected by the combined influence of different phenomena, especially in the two-phase zone where the pressure and temperature profiles are imposed by combined flow and thermal effects.

The results based on the temperature field were completed by thermodynamic and hydrodynamic considerations using the measured pressures.

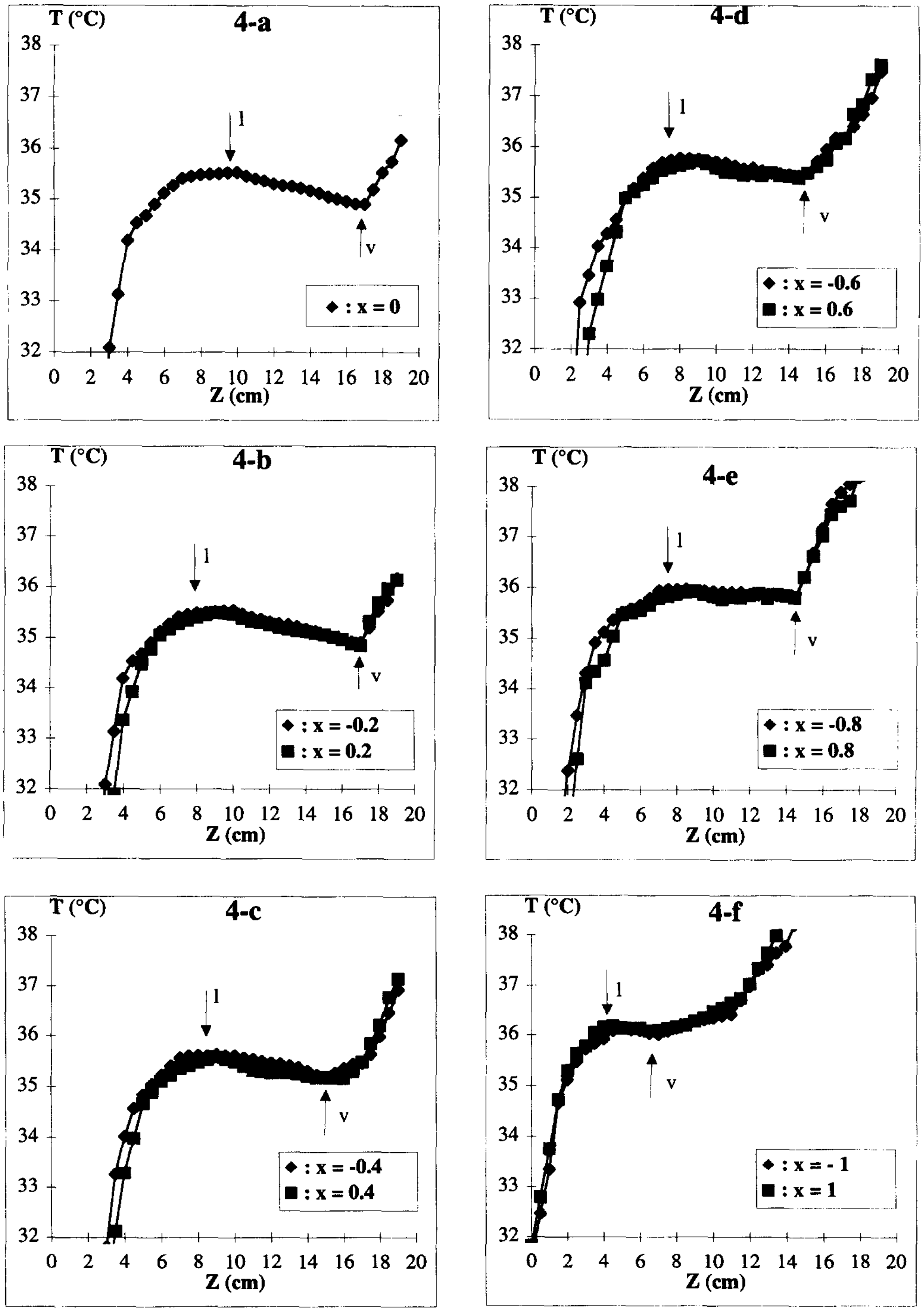

Fig. 4. Temperatures profiles along the vertical axis. These profiles are plotted in pairs (points equidistant to the centerline). On each curve, the ◆ symbol corresponds to the profile with negative abscissa and the ■ symbol to those with positive abscissa. The boundaries of the different zones are marked by the arrows: ↓ for the liquid-two-phase font and ↑ for the two-phase-vapor limit. Liquid: n-pentane ($U = 0.69\ 10^{-3}$ m s^{-1}). Heat flux applied to the plates: 5000 W m^{-2}.

3.3. *Identification of zone boundaries using pressure data*

In the liquid and vapor zones, pressure values are not dependent on temperature and there is no variation in saturation. If the flow is assumed to be one-dimensional in these zones, the pressure field can be obtained by applying Darcy's law. The inlet pressure for the liquid zone and the outlet pressure for the vapor zone serve as reference values.

The flow is assumed to be one-dimensional (in the

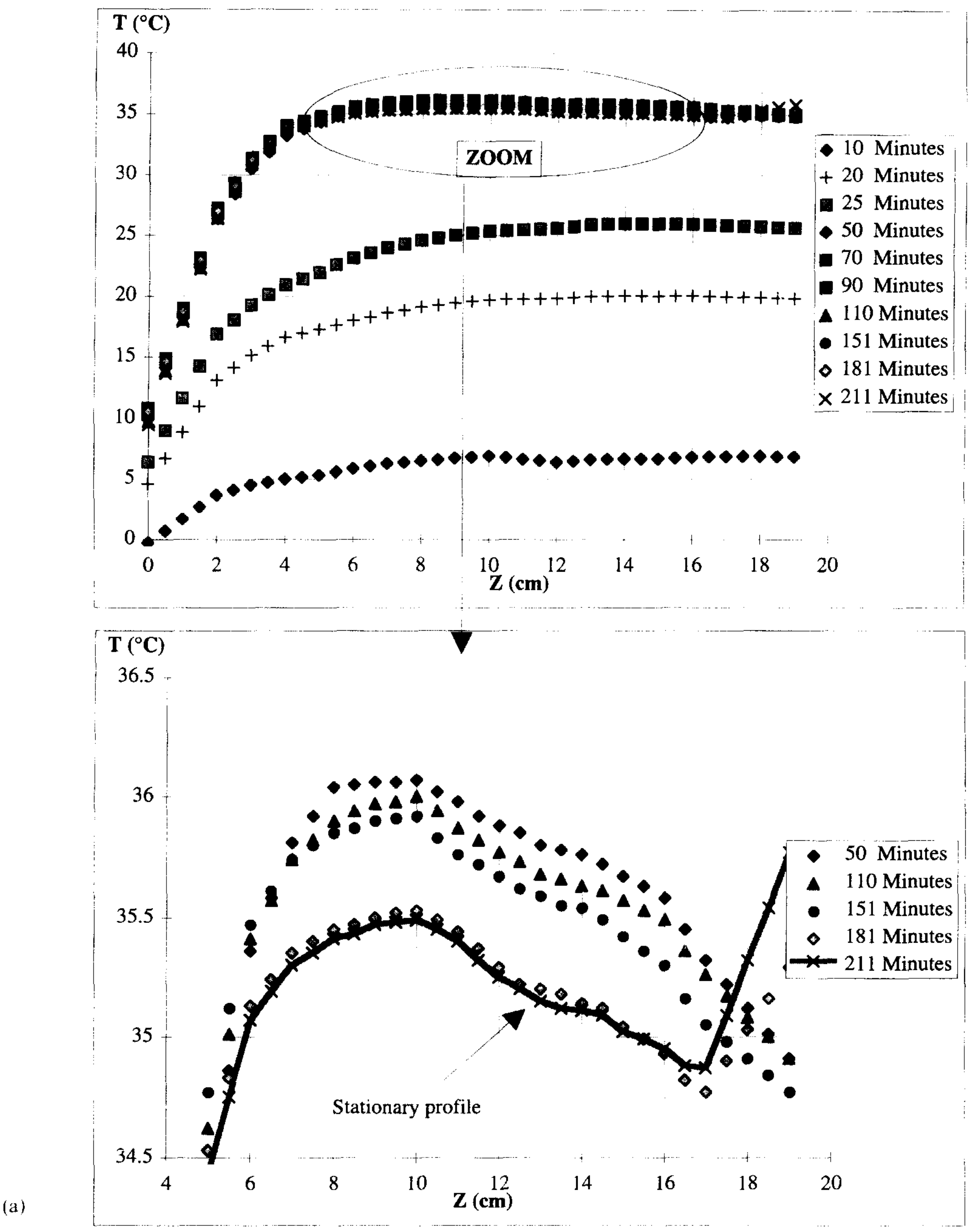

Fig. 5. Temporal evolution of the temperature profiles on the centerline along the vertical axis. Global view and detailed view around saturation temperature values. (a) Liquid: n-pentane ($U = 0.69\ 10^{-3}$ m s^{-1}). Heat flux applied to the plates: 5000 W m^{-2}. (b) Liquid: n-pentane ($U = 1.03\ 10^{-3}$ m s^{-1}). Heat flux applied to the plates: 5000 W m^{-2}. (c) Liquid: n-pentane ($U = 1.38\ 10^{-3}$ m s^{-1}). Heat flux applied to the plates: 10 000 W m^{-2}. (*Continued opposite and overleaf.*)

case of two-dimensional flow, the results obtained are quite similar), and the physical values are assumed to be constant for each of these single-phase zones. The saturation in the two-phase zone is variable and the pressure values of the liquid and vapor zones are linked by capillary pressure. In this case the general expression for the vapor pressure is

$$P_v(S,T) = P_{\text{vsat}}(T)\varnothing(S,T).$$

$\varnothing(S,T)$ is given by Kelvin's law and to develop a model of the pressure drop at the surface of the meniscus. An evaluation of this function shows that this decrease appears to be very slight for S greater than S_{irr} ($S \approx 0.01 => \varnothing(0.01,T) \approx 0.9$). In the two-phase zone the saturation is always greater than S_{irr} and the vapor pressure is dependent only on the temperature

$$P_v(T) = P_{\text{vsat}}(T). \qquad (1)$$

A capillary pressure discontinuity must exist in the two-phase zone between the liquid and the vapor

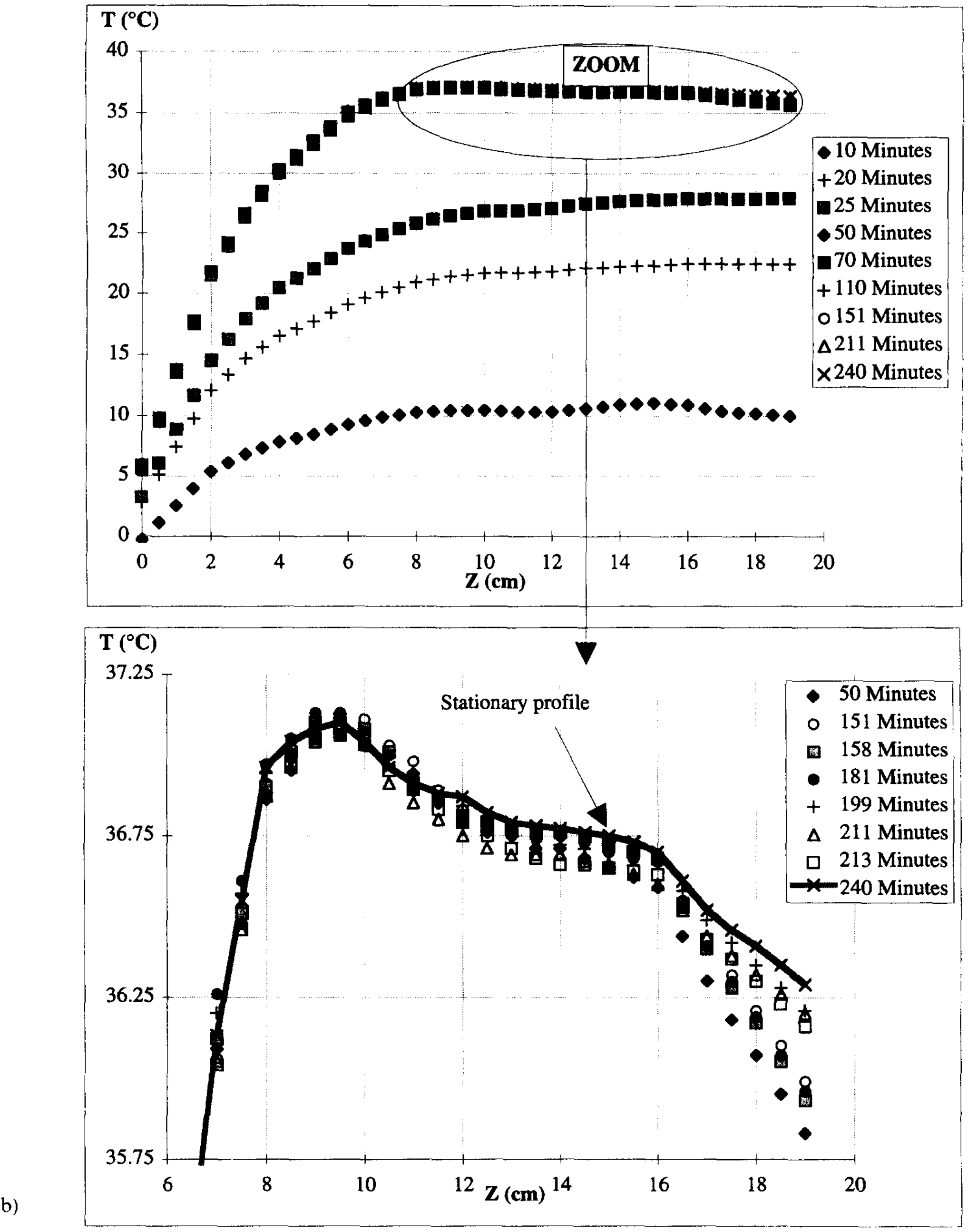

Fig. 5—*Continued.*

phases. The liquid pressure is given by the following relation:

$$P_1(S,T) = P_v(T) - P_c(S), \tag{2}$$

where P_v is the pressure of the saturated vapor and P_c the capillary pressure as determined by Leverett's law (Appendix I).

The pressure values at the liquid front, defined previously, are the same when calculated from the liquid zone or from the two-phase zone. As there are no capillary effects at the front ($S = 1$), the liquid pressure is equal to that of the saturated vapor. This pressure is also equal to the value deduced applying Darcy's law to a liquid zone. A similar approach can be applied to the vapor front.

The boundaries of the different zones are defined by the intersections of surface $P_{\mathrm{vsat}}(x,z)$ [pressure of saturated vapor at local temperature] and planes $P_l(x,z)$ and $P_v(x,z)$ [hydrodynamic pressure in single-phase zones]. $P_l(x,z) = P_{\mathrm{Vsat}}(x,z)$ represents the liquid front and $P_v(x,z) = P_{\mathrm{Vsat}}(x,z)$ the vapor front.

The pressure profiles along the central axis for each zone are plotted on Fig. 6. The hydrodynamic pressure of liquid is linear in the liquid zone.

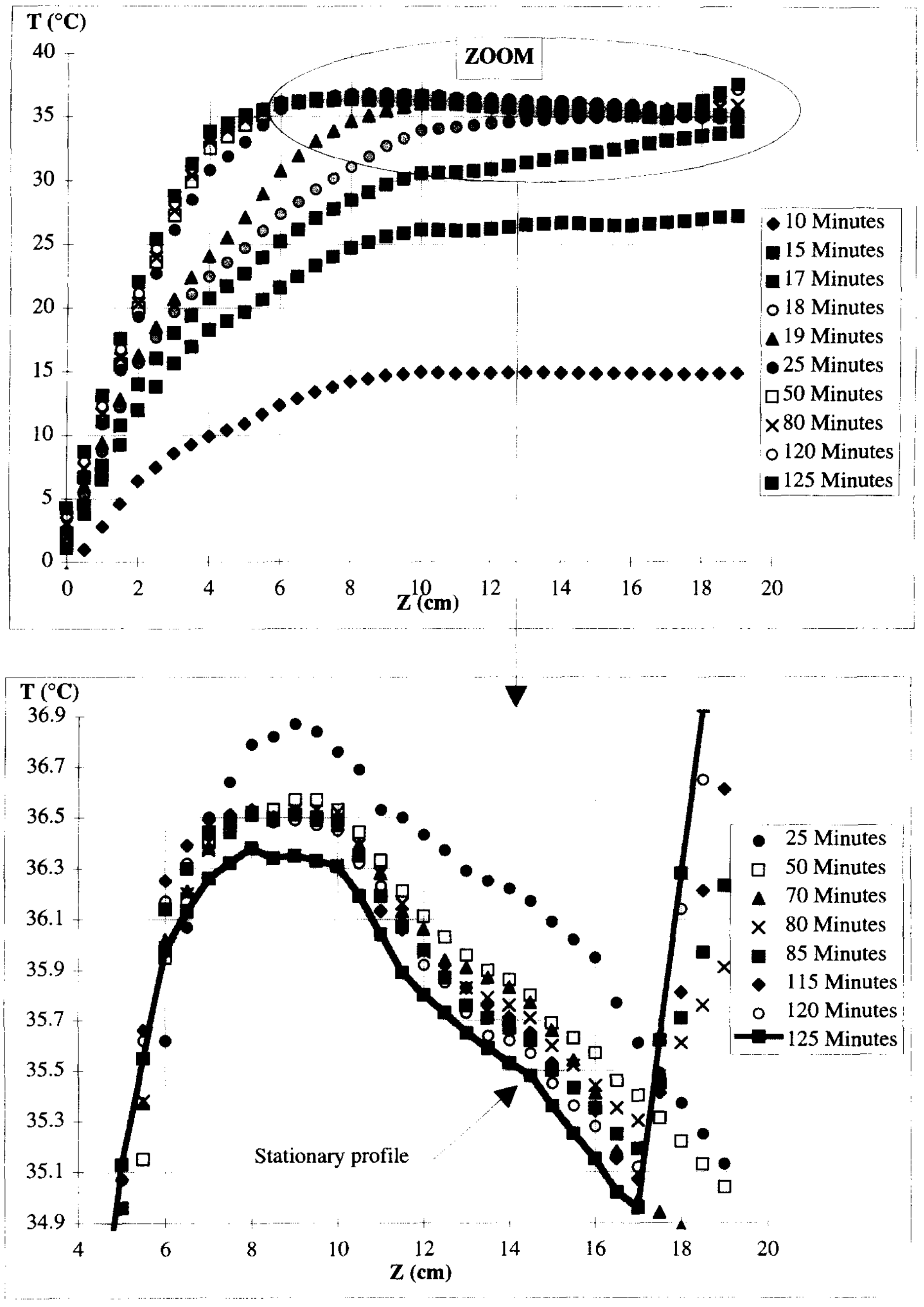

(c)

Fig. 5—*Continued.*

Both vapor and liquid hydrodynamic pressures profile on the center axis are plotted on Fig. 6, along with the pressure of the saturated vapor (thermodynamic pressure of vapor) and the calculated pressure.

Figure 6 shows the variations of the different pressures along the central axis. The pressure of saturated vapor is plotted all along the porous medium (curve: 'thermodynamic pressure of vapor'). In the liquid and vapor zone are plotted the hydrodynamic pressures deduced from Darcy's law. In the two-phase zone, the liquid pressure is calculated using the model (curve: 'calculated pressure of liquid').

This approach shows that the pressure curve intersection points correspond to the local maximum (liquid front) and minimum (vapor front) temperature values of the longitudinal temperature profiles, thus confirming the identification of the boundaries, as determined by the temperature profiles alone.

4. CALCULATION OF SATURATION FIELD

4.1. *Equations*

These experimental data allow us to describe the thermal behavior in single-phase liquid and vapor

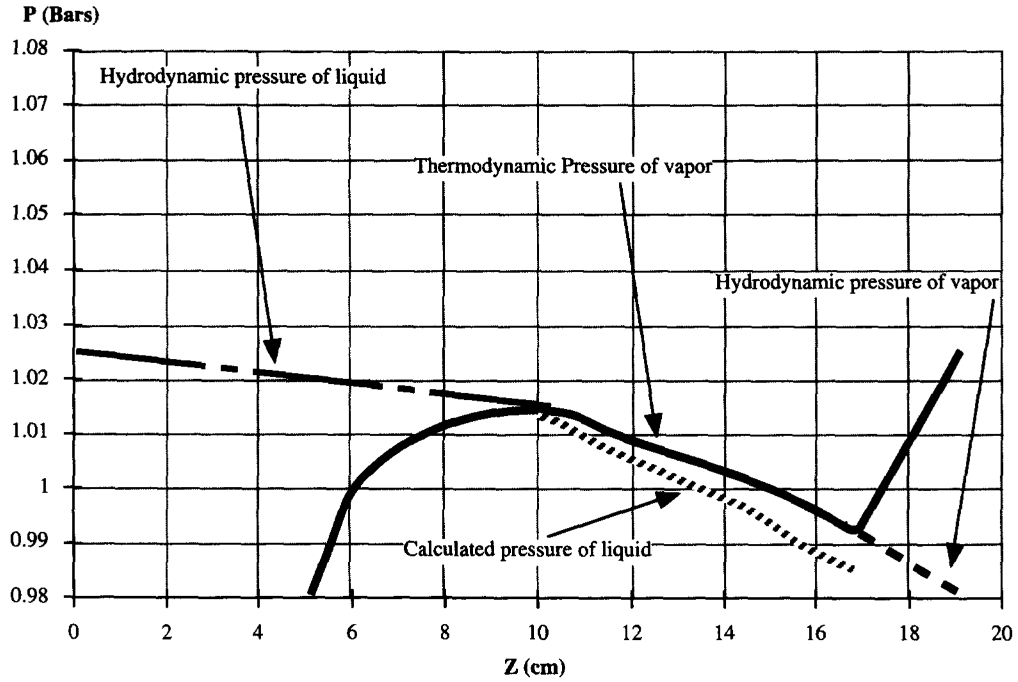

Fig. 6. Pressure profiles on the centerline along the vertical axis. The thermodynamic pressure of vapor is the saturating vapor pressure at the local temperature; the hydrodynamic pressure of both liquid and vapor zone are obtained using Darcy's law and the inlet and outlet pressure values. Liquid: n-pentane ($U = 0.69\ 10^{-3}$ m s^{-1}). Heat flux applied to the plates: 5000 W m^{-2}.

zones [12]. In the two-phase zone on the other hand, although a fine description of the temperature field is obtained, other parameters are not accessible (e.g. saturation, pressure . . .).

In order to describe this latter zone in detail, a numerical model was developed based on the established formalisms and hypotheses in this field. The following hypotheses were used:

(1) Heat and mass transfer in the porous medium can be described using a macroscopic approach. At the scale of a representative elementary volume (R.E.V.) the porous medium is considered as a consolidated medium.

(2) In a R.E.V. all phases are in local thermodynamic equilibrium.

(3) The solid phase is nondeformable and homogeneous.

(4) The vapor and liquid pressures are given by expressions (1) and (2).

(5) Due to the weak temperature variations observed in the two-phase zone, the temperature-related variations in the physical values were neglected.

The equations used are as follows:

The generalized Darcy law for the expression of fluid motion

$$\boldsymbol{\eta}_v = -\frac{k_v}{\nu_v}(\nabla P_v - \rho_v \boldsymbol{g}) \tag{3}$$

$$\boldsymbol{\eta}_l = -\frac{k_l}{\nu_l}(\nabla P_l - \rho_l \mathbf{g}). \tag{4}$$

Using equations (1) and (2), the pressure gradients of the liquid and vapor zones can be expressed as a function of temperature and of saturation.

The mass velocity of the vapor phase is deduced from equations (1) and (3)

$$\boldsymbol{\eta}_v = -\frac{k_v}{\nu_v}\left(\frac{\partial P_v}{\partial T}\nabla T + \frac{\partial P_v}{\partial S}\nabla S - \rho_v \boldsymbol{g}\right). \tag{5}$$

The same holds true for the mass velocity of the liquid phase [equation (2) and (4)]

$$\boldsymbol{\eta}_l = -\frac{k_l}{\nu_l}\left(\left(\frac{\partial P_v}{\partial T} - \frac{\partial P_c}{\partial T}\right)\nabla T + \left(\frac{\partial P_v}{\partial S} - \frac{\partial P_c}{\partial S}\right)\nabla S - \rho_l \boldsymbol{g}\right). \tag{6}$$

For an elementary representative volume, the variation in the quantity of liquid is the result of transport and production terms.

$$\varepsilon \frac{\partial \rho_l S}{\partial t} = -\nabla \cdot \boldsymbol{\eta}_l + \dot{m}_l \tag{7}$$

the same holds true for the quantity of vapor

$$\varepsilon \frac{\partial \rho_v (1-S)}{\partial t} = -\nabla \cdot \boldsymbol{\eta}_v + \dot{m}_v. \tag{8}$$

By adding equations (7) and (8), we obtain

$$\varepsilon\frac{\partial(\rho_l S+\rho_v(1-S))}{\partial t} = -\nabla\cdot(\boldsymbol{\eta}_l+\boldsymbol{\eta}_v)+\dot{m}_l+\dot{m}_v. \tag{9}$$

The production terms for the liquid and the vapor are necessarily opposite, as the formation of a certain quantity of vapor corresponds to the disappearance of an equal quantity of liquid; thus

$$\dot{m}_l = -\dot{m}_v. \tag{10}$$

The mass equation is expressed as follows:

$$\varepsilon(\rho_l-\rho_v)\frac{\partial S}{\partial t} = -\nabla\cdot(\boldsymbol{\eta}_l+\boldsymbol{\eta}_v). \tag{11}$$

Replacing the mass fluxes by their expressions, we obtain

$$\varepsilon(\rho_l-\rho_v)\frac{\partial S}{\partial t} = \nabla\cdot((KM_{\mathrm{PT}}+KM_{\mathrm{LT}})\nabla T + (KM_{\mathrm{PS}}+KM_{\mathrm{LS}})\nabla S+KM_{\mathrm{GS}}\boldsymbol{g}) \tag{12}$$

where

$$KM_{\mathrm{PT}} = \left(\frac{k_l}{v_l}+\frac{k_v}{v_v}\right)\frac{\partial P_v}{\partial T}$$

$$KM_{\mathrm{PS}} = \left(\frac{k_l}{v_l}+\frac{k_v}{v_v}\right)\frac{\partial P_v}{\partial S}$$

$$KM_{\mathrm{LS}} = -\frac{k_l}{v_l}\frac{\partial P_c}{\partial S}$$

$$KM_{\mathrm{LT}} = -\frac{k_l}{v_l}\frac{\partial P_c}{\partial T}$$

$$KM_{\mathrm{GS}} = -\frac{k_l\rho_l}{v_l}-\frac{k_v\rho_v}{v_v}.$$

In reality, saturation-related pressure variations (P_v) are negligible for saturation levels above the irreducible saturation level (1). The mass equation can thus be reduced to

$$\varepsilon(\rho_l-\rho_v)\frac{\partial S}{\partial t} = \nabla\cdot(KM_{\mathrm{PT}}\nabla T)+\nabla\cdot(KM_{\mathrm{LS}}\nabla S) + \frac{\partial KM_{\mathrm{GS}}}{\partial S}\boldsymbol{g}\cdot\nabla S. \tag{13}$$

This equation reveals two independent variables (T and S). In order to simplify the overall equation, the temperature then is treated as a known source term Q_{T} (calculated from the experimental temperature field). The mass equation that is used takes the following form for stationary regime:

$$\nabla\cdot(KM_{\mathrm{LS}}\nabla S)+\frac{\partial KM_{\mathrm{GS}}}{\partial S}\boldsymbol{g}\cdot\nabla S = Q_{\mathrm{T}}. \tag{14}$$

4.2. *Numerical method and results*

Equation (14) is resolved using a finite-element method that is particularly well suited for the description of the two-phase zone's complex shape [Fig. 7(a)]. This method actually consists of dividing the space under study into elements which form a grid. The elements are adjusted locally to the shape of the zone [17].

The differential equation (14) is then integrated into each of the zones and the solution is approximated using interpolation functions defined for each element (see Appendix II). After dividing the space into discrete elements, a nonlinear algebraic system is obtained and then resolved using the Newton–Raphson method.

Figure 7 shows an example of the shape of a two-phase zone obtained experimentally and the grid which was used in this case. The grid is composed of 443 isoparametric linear elements (Q4: four nodes quadrilateral and T3: three nodes triangle) and 448 nodes. The Q_{T} term is calculated for each of the nodes in the grid using the experimental temperature field [Fig. 8(b)]. The following saturation boundary conditions are used (Fig. 7):

(1) for the liquid front, the saturation is equal to 1;

(2) at the wall, the saturation varies in a linear manner from 1 to the irreducible saturation value (S_{irr});

(3) at the vapor front, the saturation value used is equal to S_{irr}.

The equation (14) is strongly nonlinear; the coefficients are a function of saturation, varying by several orders of magnitude. In order to obtain a rapid convergence, the Newton–Raphson method was used as it is particularly well adapted to this sort of equation, but it does require an initial solution close to the solution. To obtain such a point, the expression is made linear using constant coefficients corresponding to an average saturation value ($S = 0.5$). This equation system is resolved using a Gaussian-elimination direct method [18]; from this initial solution, the nonlinear equation set is then resolved; convergence is obtained after approximately 20 iterations.

The experimental temperature field used to calculate the heat source term and the corresponding calculated saturation field are shown in Fig. 8.

The iso-saturation lines are clearly stretched in the main flow axis direction. Consequently, the saturation variations are straight in the heat flux direction. There is a decrease from 1 down to S_{irr} on 1 cm, while in the ZZ-direction the saturation decreases progressively for about 10 cm.

The saturation profiles in the XX-direction do not present any notable inflection; they resemble one another regardless of the distance and are straighter as the distance to the liquid front decreases (Fig. 9). In the ZZ-direction, the profiles show a flattening of the saturation profile. This trend is all the more pronounced (occurring at higher saturation values) as we move away from the wall (Fig. 10).

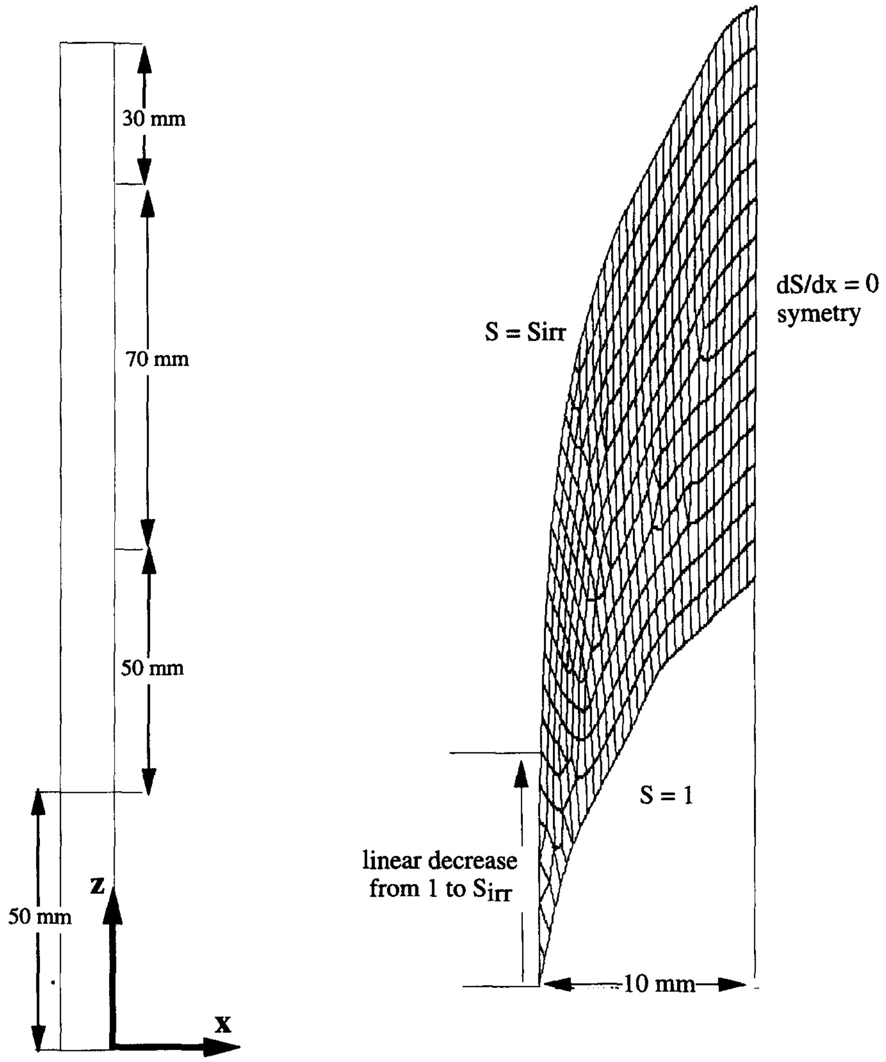

(a)
Position and size of
the diphasic zone

(b)
Finite elements mesh and
boundary conditions

Fig. 7. Liquid: n-pentane ($U = 0.69\ 10^{-3}$ m s^{-1}). Heat flux applied to the plates: 5000 W m^{-2}. (a) Shape of two phase zone at steady state regime. (b) Finite-element grid for the two-phase zone and boundary conditions. This grid is composed of 443 linear elements (Q4 and T3) and 448 nodes.

The complexity of the phenomena induced by the combined thermal, capillary and phase-change effects makes it difficult to interpret the distribution of saturation values with precision. Several qualitative explanations can, however, be advanced. The selected experimental configuration produces two distinct effects of primary importance; along the XX-axis, the thermal effects due to the imposed heat flux are primordial, whereas along the ZZ-axis, the forced flow effects are dominant.

Along the ZZ-axis, the fluid flow is determined by thermal, capillary and forced convection effects coupling; in the two-phase flow both phases flow in the same direction, whereas along the XX-axis they flow in opposite directions.

The saturation field is used to calculate the pressure field for the liquid zone. This field is shown in Fig. 6, which also represents the evolution of pressure loss along the central axis of the apparatus. This combined experimental and numerical approach makes it possible to describe with precision the values characterizing this phenomenon on a macroscopic scale.

5. CONCLUSION

The experimental analysis based on the evaluation of temperature over space and time revealed three

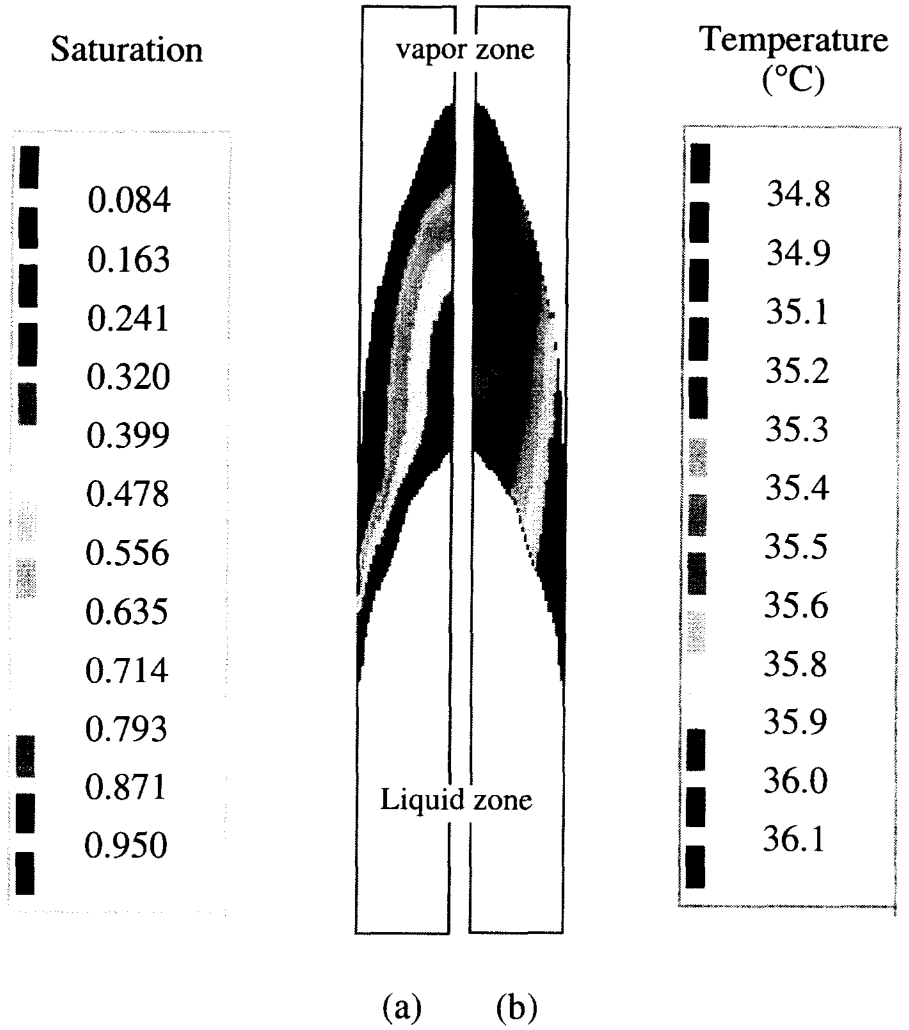

Fig. 8. Representation of the calculated saturation field and the experimental temperature field in the median plane perpendicular to the heating plates. (a) Saturation field (numerical). (b) Temperature field (experimental). These temperatures are obtained with the following conditions: liquid, n-pentane ($U = 0.69$ 10^{-3} m s^{-1}). Heat flux applied to the plates: 5000 W m^{-2}.

distinct zones, corresponding to the different states of the fluid:

(1) a liquid zone Z_l near the column inlet;
(2) a two-phase zone Z_d;
(3) a vapor zone Z_v near the outlet.

The temperature in the two-phase zone is seen to decrease, forming an *N*-shaped curve, probably resulting from combined flow and phase-change effects.

The boundaries of the zones were determined with great precision by associating two approaches. The first relies on the use of the temperature fields and the second uses the pressure data to validate these first results.

In the liquid and vapor zones, the pressure profiles are established by applying Darcy's law to inlet and outlet pressure readings. In the two-phase zone, the vapor pressure is considered equal to that of the saturated vapor. The different temperature measurements were completed using a numerical simulation of heat and mass transfer with phase change. This allows the saturation to be calculated from the mass equation (taking into account capillary effects and temperature variations). The pressure of the liquid phase is then deduced using Leverett's law (which gives the capillary pressure as a function of the calculated saturation values).

This work will be continued by carrying out pressure and saturation measurement in the two-phase zone. The numerical model will be extended to the resolution of the combined mass-energy equation. This will allow the different parameters characterizing

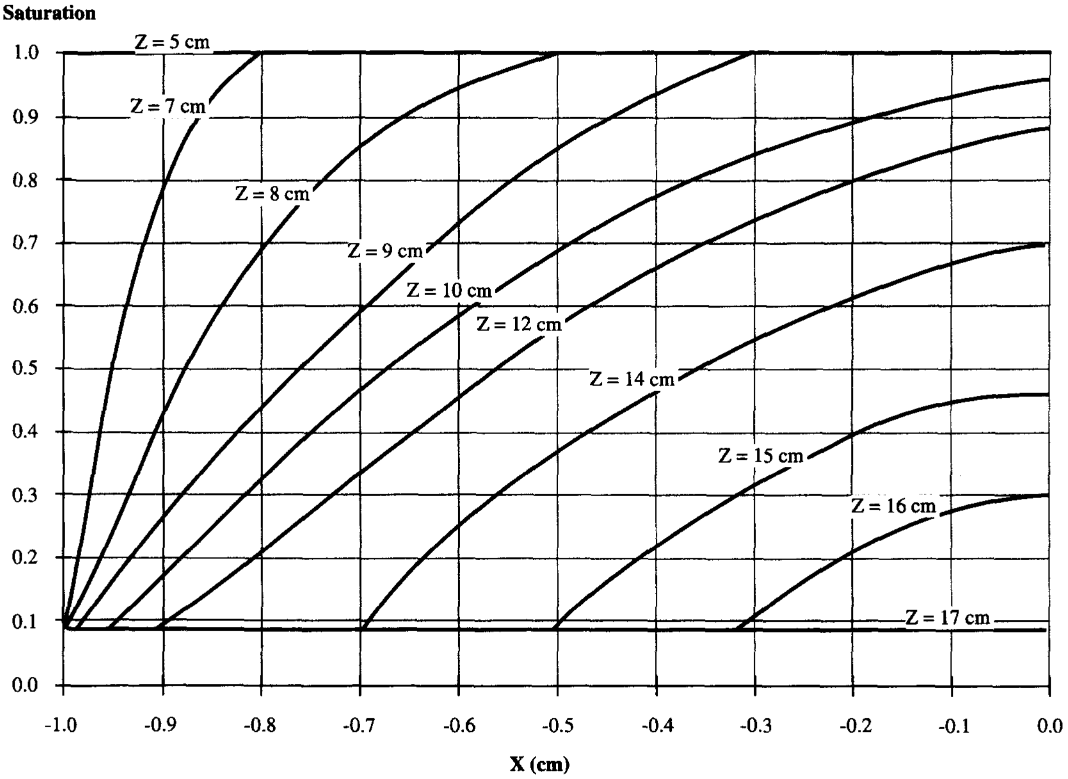

Fig. 9. Numerical saturation profiles along the horizontal axis *XX* in the median plane perpendicular to the heating plates for several *z* values.

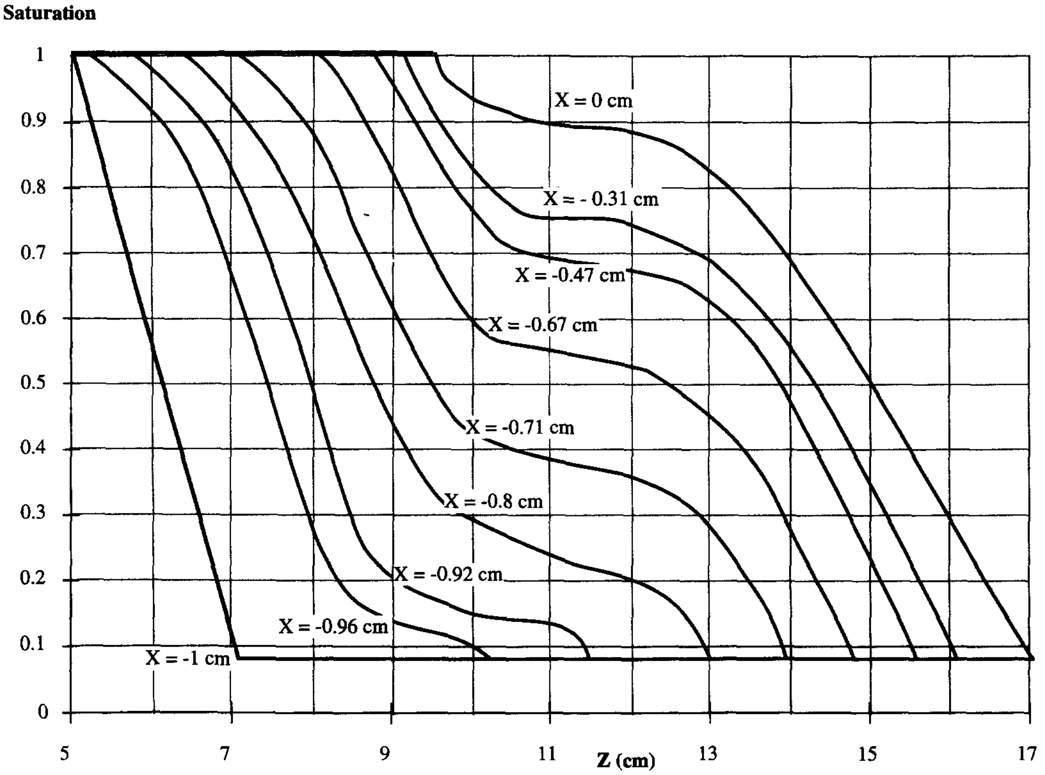

Fig. 10. Numerical profiles of the saturation in the *ZZ*-direction for several abscissa.

boiling mechanism in porous media with forced flow to be described.

REFERENCES

1. K. E. Torrance, Boiling in porous media, *ASME/JSME Thermal Engineering Joint Conference Proceedings* (Edited by Y. Mori and W.-J. Yang), Vol. 1, pp. 593–606. ASME/JSME, New York (1983).
2. C. H. Sondergeld and D. L. Turcotte, An experimental study of two-phase convection in a porous medium with applications to geological problems. *J. Geophys. Res.* **82,** 2045–2053 (1977).
3. H. Bau and K. E. Torrance, Boiling in low-permeability porous materials, *Int. J. Heat Mass Transfer* **25,** 45–55 (1982).
4. C. H. Sondergeld and D. L. Turcotte, Flow visualisation studies of two phase convection in a porous medium with applications to geological problems, *Pure Appl. Geophys.* **117,** 321–330 (1978).
5. G. Schubert and J. M. Strauss, Two-phase convection in a porous medium, *J. Geophys. Res.* **82,** 3411–3421 (1977).
6. G. Schubert and J. M. Strauss, Gravitational stability of water over steam in vapor dominated geothermal systems. *J. Geophys. Res.* **85,** 6505–6512 (1980).
7. M. J. O'Sullivan, Geothermal reservoir simulation, *Int. J. Energy Res.* **9,** 319–332. [An edited version was reprinted in *Applied Geothermics* (Edited by M. Economides and P. Ungemash). Wiley, New York (1987).]
8. M. J. O'Sullivan, Convection with boiling in porous layer. In *Convective Flows in Porous Media* (Edited by R. A. Wooding and I. White), pp. 141–155. Wellington, NZ (1985).
9. P. S. Ramesh and K. E. Torrance, Numerical algorithm for problems involving boiling and natural convection in porous materials, *Numer. Heat Transfer B* **17,** 1–24 (1990).
10. A. S. Naik and V. K. Dhir, Forced flow evaporating cooling of a volumetrical heated porous layer, *Int. J. Heat Mass Transfer* **25,** 541–552 (1982).
11. V. X. Tung and V. K. Dhir, Finite element solution of multi-dimensional two-phase flow through porous media with arbitrary heating conditions, *Int. J. Multiphase Flow.* **16,** 985–1002 (1990).
12. S. Cioulachtjian, Analyse des transferts de chaleur avec changement de phase dans un milieu poreux non consolidé. Etude experimentale et modélisation, thèse de l'I.U.S.T.I., Université de Provence, Marseille, 168 pp (1989).
13. J. Bear, *Dynamics of Fluids in Porous Media.* American Elsevier, New York (1972).
14. S. Cioulachtjian, L. Tadrist, R. Santini, R. Occelli and J. Pantaloni, Etude des transferts de chaleur dans un milieu poreux. Cas d'un Liquide en Ecoulement, *Rev. Gen. Therm. Fr.* **338,** 85–90 (1990).
15. O. Rahli, S. Cioulachtjian, L. Tadrist and R. Santini, Boiling in porous media—an experimental and numerical analysis, *ASME/ECOS'92. Proceedings of the International Symposium ECOS'92; On Efficiency, Costs, Optimization and Simulation of Energy Systems,* Zaragoza, Spain pp. 515–520; 15–18 June (1992).
16. M. Kaviany, *Principles of Heat Transfer in Porous Media, Mechanical Engineering Series.* Springer, Berlin (1992).
17. G. Datt and G. Touzot, *Une Presentation de Méthode des Éléments Finis.* Maloine, Paris (1984).
18. T. Lascaux, *Analyse Numérique Matricielle Appliquée à l'Art de l'Ingenieur.* Masson, Paris (1981).
19. K. S. Udell, Heat transfer in porous media heated from above with evaporation, condensation and capillary effects, *J. Heat Transfer Trans. ASME* **105,** 485–491 (1983).
20. K. S. Udell, Heat transfer in porous media considering phase change and capillarity—the heat pipe effect, *Int. J. Heat Mass Transfer* **28,** 485–495 (1985).
21. I. Fatt and W. A. Klikoff, Effect of fractional wettability on multiphase flow through porous media, Note no. 2043, *AIME Trans.* **216,** 246 (1959).

APPENDIX I
PHYSICAL VALUES

Using correlations based on experimental data, Leverett's law is expressed [13, 16, 19, 20] as

$$P_c(S) = \sigma \sqrt{\frac{\varepsilon}{K_{sat}}}\, F(S),$$

where $F(S) = 1.417\ (1-s)\ -2.12\ (1-s)^2 + 1.263\ (1-s)^3$ to express P_c in Pascal.

The permeabilities of the liquid and vapor phases were obtained using conventional expressions [21]

$$K_l = K_{sat}\left(\frac{S-S_{irr}}{1-S_{irr}}\right)^3 \quad K_v = K_{sat}\left(\frac{1-S}{1-S_{irr}}\right)^3,$$

where K_{sat} is the intrinsic permeability of the medium.

The following thermo-physical properties were used for the bed of bronze spheres through which pentane flows:

kinematics viscosity of the liquid ν_l	$4.09\ 10^{-7}$ m^2 s^{-1}
kinematics viscosity of the vapor ν_v	$2.37\ 10^{-6}$ m^2 s^{-1}
density of the liquid ρ_l	606 kg m^{-3}
density of the vapor ρ_v	3.1 kg m^{-3}
permeability K_{sat}	$21\ 10^{-12}$ m^2
porosity ε	0.3975
interface tension σ	$13.12\ 10^{-3}$ N m^{-1}
irreducible saturation S_{irr}	0.084
saturating vapor pressure P_{vsat}	$14.718+74.814\ T-30.785\ T^2+5.769\ T^3$ bars with T in °C.

APPENDIX II
FINITE-ELEMENT FORMULATION OF THE PROBLEM

An S function was sought in study zone Ω, such that it would match equation (14) and boundary conditions at the Γ boundary.

The total Ω zone is discretized by dividing it into a grid of finite elements. Each element is connected at several points called nodes. At each node, the saturation value is treated as the unknown nodal value. Within an element (e), the variations of $S(x, y)$ are expressed in terms of its nodal values S^e as follows:

$$S^e(x,y) = \sum_{i=1}^{nnel} N_i(x,y) S^{ei} = \langle N(x,y) \rangle \{S^e\}, \tag{A1}$$

where superscript e denotes quantities pertaining to an element; *nnel* is the number of nodes in the element; N_i is a polynomial function (called the shape function) expressed of spatial coordinates (x, y) and formulated such that, if evaluated at the ith node, it gives a unity value and a zero value at the other nodes; and S^{ei} denotes the nodal saturation value at the ith node.

$R(S)$ is called the residual quantity

$$R(S) = \nabla \cdot \left(KM_{LS} \boldsymbol{\nabla} \langle N \rangle \{S^e\} \right) + \frac{\partial KM_{GS}}{\partial S} \boldsymbol{g} \cdot \boldsymbol{\nabla} \langle N \rangle \{S^e\} - Q_T. \tag{A2}$$

The pondered residue method consists in seeking S functions that cancel out the integral form

$$I = \int_{\Omega} \langle \Psi \rangle \{R(S)\} \, \mathrm{d}\Omega = 0. \tag{A3}$$

The polynomial approximation introduced in the weak integral formulation I of the problem gives

$$I = \sum_{c=1}^{\text{Nelt total}} \int_{\Omega_e} \langle \Psi^* \rangle \{N\} \left(\nabla \cdot (KM_{\mathrm{LS}} \nabla \langle N \rangle \{S^e\}) + \frac{\partial KM_{\mathrm{GS}}}{\partial S} \boldsymbol{g} \cdot \nabla \langle N \rangle \{S^e\} - Q_{\mathrm{T}} \right) \mathrm{d}\Omega_e. \tag{A4}$$

Integrating by parts gives

$$I \langle \Psi^* \rangle [\mathrm{K}] \cdot \{S\} - \{VF\}, \tag{A5}$$

where

$$[K] = \sum_{e=1}^{nel} ([K_e^{\mathrm{d}}] + [K_e^{\mathrm{cv}}]) \tag{A6}$$

$$[K_e^{\mathrm{c}}] = \int_{\Omega_e} \left[\left\langle \frac{\partial N_e}{\partial x_i} \right\rangle \right]^{\mathrm{T}} [KM_{\mathrm{LS}}] \left[\left\langle \frac{\partial N_e}{\partial x_i} \right\rangle \right] \mathrm{d}\Omega_e$$

$$[K_e^{\mathrm{cv}}] = \int_{\Omega_e} \{N_e\} \langle N_e \rangle \left\{ \frac{\partial KM_{\mathrm{GS}}}{\partial S} \boldsymbol{g} \right\} \mathrm{d}\Omega_e \tag{A7}$$

and

$$\{VF\} = \sum_{e=1}^{nel} (\{V_e^{\mathrm{Q}}\} + \{V_e^{\mathrm{cl}}\}) \tag{A8}$$

$$\{V_e^{\mathrm{Q}}\} = \int_{\Omega_e} - \{N_e\} Q_{\mathrm{T}} \, \mathrm{d}\Omega_e, \tag{A9}$$

where

$$\{V_e^{\mathrm{cl}}\} = \int_{\Gamma_e} - \{N_e\} \left[\left\langle \frac{\partial N_e}{\partial x_i} \right\rangle \right]^{\mathrm{T}} [KM_{\mathrm{LS}}] \left[\left\langle \frac{\partial N_e}{\partial x_i} \right\rangle \right] \mathrm{d}\Gamma_e. \tag{A9}$$

At this point, we resolve the nonlinear $I = 0$ system using the Newton–Raphson method.